

Magnetic field stabilization of low current DC arc discharge in cross flow in argon gas at atmospheric pressure – a numerical modelling study

V Ivanov¹, Ts Paunsk¹, Kh Tarnev² and St Kolev¹


¹ Faculty of Physics, Sofia University, 5 James Bourchier Boulevard, 1164 Sofia, Bulgaria

² Department of Applied Physics, FAMI, Technical University-Sofia, 8 Kl. Ohridski Blvd., Sofia BG-1000, Bulgaria

E-mail: vladislavvi@phys.uni-sofia.bg, skolev@phys.uni-sofia.bg

Abstract.

In this work we study the effect of an external magnetic field and gas flow on the properties of a low current DC (gliding) arc discharge in argon at atmospheric pressure. We consider a cross flow configuration, in which argon gas flows perpendicularly to the arc current, while the external magnetic field is perpendicular to both the arc current and the gas flow. The study is based on a 2D numerical fluid plasma model of the discharge, coupled with a gas flow model based on the Navier-Stokes equations and a gas thermal balance equation. In the examined configuration, a stabilized arc is achieved by having the ExB drift acting in opposite direction to the gas flow, i.e. the Lorentz force pushing the arc against the gas flow.

The numerical model was implemented into a finite element simulation, using the Comsol Multiphysics  (version 5.3) package. The results proved that a magnetically stabilized arc can be sustained and that the examined configuration can be used for effective gas treatment. The analysis of the simulation data helped to answer multiple questions, related to arc stability, the energy density distribution in the arc, and the macroscopic properties of the system as a whole. The results show a significant influence of the walls on the arc stabilization, while in the case of walls positioned very far from the arc, i.e. unbounded channel, the arc becomes a source of a fluid instability, causing vortex shedding.

In general, this study provides insight on the interaction between the gas flow and the arc in a strong magnetic field. The model presented here has the potential to further the understanding of magnetically stabilized discharges and to become a basis for developing similar studies of more complex gases.

Keywords: plasma, arc discharge, DC discharge, magnetic confinement, magnetic stabilization, vortex shedding, vortex street

Submitted to: *Plasma Sources Sci. Technol.*

1. Introduction

The electric arcs are well known and studied type of discharges, used extensively in the industry for more than a century. While they are thoroughly examined in various classical configurations, we still face some new specific configurations which show unexpected and complex behavior.

In this work we study a configuration of low current (below 1 A) DC arc in cross gas flow in bounded domain and stabilized by constant in time magnetic field perpendicular to both the arc current and the gas flow. Arc discharges in the low DC current range (tens of milliamperes) have their application in gas treatment, and in particular for CO₂ gas dissociation [1,2]. The low currents allow for the control of the level of plasma non-isothermality, the amount of plasma ionization, and the amount of heat transferred to the gas from the plasma. All of these parameters are crucially important in the field of processing, and especially in the case of CO₂ dissociation. The method of magnetic field stabilization provides the ability to control the velocity of the arc relative to the gas, and also allows to establish and maintain a steady (in time), localized (in space) arc channel, with a quasi constant power and therefore constant ionization.

As a prototype, we consider a gliding arc discharge [3] with diverging flat electrodes, which is equipped with permanent magnets, providing magnetic field perpendicular to the electrodes and the arc. Due to the magnetic field, the arc is stabilized at certain position, where the Lorentz force is balanced by the gas flow drag. This study is motivated by the development of a more efficient setup for gas treatment by low current arcs in our laboratory at Sofia University. Our target is to build a magnetically stabilized arc which can treat significant fraction of the flowing gas.

The use of magnetic field to modify the arc motion and properties is an old method. Even in the beginning of 20th century it was used in the Birkeland-Eyde [4] reactors for production of nitrates. The electrical power of a typical industrial reactor was in the megawatt range. Nowadays the use of arcs with magnetic field control is extended towards low current and small size devices like gas flow actuators [5], despite the relatively small Lorentz force at low currents. In the context of gas treatment, several different discharge configurations with a magnetic field exist. Notable developments are the above mentioned Birkeland-Eyde process and setups based on cylindrical geometry in which the electrodes are in coaxial configuration (concentric), the gas flow and the magnetic field are in axial direction (parallel to the electrodes) [6–11]. The arc is ignited between the concentric electrodes. Since the magnetic field is perpendicular to the arc current, the Lorentz force acts on the arc by pushing it in azimuthal direction and thus resulting in arc rotation. The nonhomogeneous magnetic field topology also results in certain quasi-stabilization of the arc at the discharge outlet, i.e. rotation in a disk. Another interesting application is the use of a magnetic field in DC gliding arc discharges with flat diverging electrodes [12]. The aim of this setup is to additionally push the arc (in addition to the gas drag), and thus to increase its velocity with respect to the gas flow. In this way the frequency of the gliding arc cycle of arc ignition and extinguishing is increased. The use of a magnetic field also allows for a significant increase in the maximum arc length.

The above mentioned setups impose the Lorentz force either in direction perpendicular to the gas flow [8–11], or downstream - along the gas velocity and

as a result, they cause additional displacement of the arc. In this work, we study a configuration in which the Lorentz force and the gas flow drag are in opposite directions and the arc is stabilized at a position where both forces become equal in magnitude. We use the term stabilization to describe the process of reaching an equality between the drag force experienced by the arc (from the interaction with the gas) and the magnetic force, at which point a localized arc can be achieved, with steady parameters in time. The working gas is argon at atmospheric pressure. In addition, our configuration considers a bounded domain (see figure 1), with distance between the walls in the same order of magnitude as the arc diameter. Again, this is not a new development and similar configurations were studied in the past [6, 13–16]. In [15], the setup was also bounded with small distance between the walls but the pressure was much lower (few Torr). In the above mentioned studies, the balance between the magnetic force and gas flow drag was examined and it was concluded that the experimental data is well described by the equality of the Lorentz force and the aerodynamic drag for a rigid cylinder, which can be written for the force per unit length of the arc as [6, 16]:

$$IB = (1/2)C_D\rho U^2 d, \quad (1)$$

where d is the diameter of the arc column perpendicular to the gas flow, ρ is the gas density and U is the gas velocity undisturbed by the arc (far from the arc or in front of the arc), I is the arc current, B is the magnetic field value and C_D is the aerodynamic drag coefficient. It is important to note however that all these studies were carried with relatively high current arcs (above several tens of Amperes) and with arcs well stabilized by the magnetic field. The arc appears as a body in gas flow with a significant Reynolds number and at certain conditions induces a gas flow instability in the form of a vortex street (Kármán vortex street). The instability itself is causing variation of the gas pressure acting on the arc in direction perpendicular to the gas flow and the arc current and thus the arc starts to vibrate (transverse motion) which causes the amplitude of the gas instabilities to become even larger. This phenomenon tends to amplify the effective (averaged) drag coefficient C_D and to cause stronger mean drag on the arc.

While the flow-induced vibration of rigid bodies in fluids is well studied (for example in [17]), there seem to be only a few studies considering similar effects on plasma arcs. Our search for similar studies led only to one mention in [18], where it is written: "The transverse blowing velocities with this configuration were limited to values below 60 frames per second. Above this velocity erratic anode behavior occurred and severe arc instabilities were present below the top locator". We are not completely sure if the observed behavior in [18] has the same nature as the one considered in our study.

This paper has the following structure: In section 2 we describe the developed numerical model, with some additional details also given in the appendices. In section 3, we present the obtained results and discuss the observed arc behavior. The results show the influence of the distance between the discharge walls on the arc stabilization and the effect of the different gas velocities on the macroscopic parameters of the arc. Lastly, the conclusions are given in section 4.

2. Model description

This model is partially based on previously developed by one of the coauthors models [19–22], considering quasi-neutral plasma, however with some significant amendments which are worth noting here: (1) The equations are properly derived for the case of a constant in time magnetic field starting from the two term approximation of the Boltzmann equation and given here within the approximation of strong collisions; (2) The current conservation equation accounts for the diffusion currents and the currents related to the $\mathbf{E} \times \mathbf{B}$ drift; (3) in the balance equations, the term proportional to the $\nabla \cdot \mathbf{u}_g$ (\mathbf{u}_g is the gas velocity) is taken into account within the particle and energy balance equations, since it was found that for the considered configuration, it becomes significant; (4) the friction between the charged species and the gas is expressed separately for every particle type and their sum forms the total volume drag force on the gas; (5) the boundary conditions are slightly modified in order to account for the magnetic field effects.

2.1. Spatial configuration

The developed model is 2D in a Cartesian coordinate system, and considers a cross section of the positive column of the arc. The arc is assumed to be stabilized between two electrodes at a large enough distance, so that the effects of the electrode regions are ignored. In our case we consider a distance of 2 cm but this is irrelevant to most of the obtained results and used only for the calculation of global parameters like the total arc power for example. Moreover, in the simulations of a non-stabilized arc (to be discussed in the text), the arc is allowed to move freely along the electrodes and thus any effects of arc bending are ignored. In addition, the region around the arc is bounded with nonconductive walls at room temperature. There is a gas flow in the domain, perpendicular to the arc current and parallel to the electrodes. Finally, there is magnetic field created by permanent magnets, which is perpendicular to the arc current and the gas flow, i.e. it is assumed that the magnets lie on the dielectric walls.

As a consequence of the above considerations, the domain Ω is defined as a rectangle in the XY plane, with a width W_D and height H_D . The arc motion is limited to the domain area. The four boundaries of the domain are named W_T , W_R , W_B and W_L , as seen in figure 1a.

The maximum values for the electric field, the magnetic flux density and gas flow velocity are typical [23, 24] for the kind of discharge under investigation here, and are chosen to be in accordance with an actual experimental device, which we are currently running tests on.

Gas velocity distribution In our model, the gas velocity and pressure are computed through the Navier-Stokes equations for compressible flow, as shown in section 2.4. The chosen maximum values of the inlet gas velocity are in accordance with our experiment. From our lab equipment we get a measurement for the exact flow rate of a gas nozzle. Through a separate fluidodynamic simulation, which also accounts for the drag of the arc on the gas, we are able to compute the corresponding gas velocity distribution in the region just ahead of the arc (upstream). This region corresponds to the bottom boundary of our simulated domain. The inlet flow velocity has a parabolic profile in the x -direction (shown in figure 1b), and has a maximum in the middle of the domain region ($x = 0$). This variation in the gas velocity distribution accounts



Figure 1: Diagram of the model spatial configuration: (a) boundaries and dimensions; (b) magnetic field vector \mathbf{B} , electric field vector \mathbf{E} , profile of the gas velocity \mathbf{u}_g .

for the friction with the side walls W_L and W_R and corresponds to a fully developed laminar flow. The boundary condition on the top boundary W_T is that of an outlet at fixed pressure and no backflow.

Spatial distribution of the electric and magnetic fields The external electric field \mathbf{E} and the magnetic field $\mathbf{B}(x, y)$ are perpendicular to each other at every point (x, y) in Ω , and have the following components:

$$\mathbf{E} = [0, 0, E_z(x, t)], \mathbf{B} = [B_x(y), 0, 0].$$

The non-zero transverse z -component of the electric field has a Gaussian profile in the x direction in the form:

$$\begin{aligned} E_z(x, y, t) &= \frac{V_c(t)}{d_z} S_E(x), \\ S_E(x) &= 0.65 \exp \left[-\frac{1}{2} \frac{x^2}{(6 \text{ (mm)})^2} \right] + \\ &+ 0.35 \exp \left[-\frac{1}{2} \frac{x^2}{(20 \text{ (mm)})^2} \right] \end{aligned} \quad (2)$$

where $V_c(t)$ is the cathode potential and d_z is the inter electrode distance in the z -direction. The spatial distribution of the electric field intensity, described by the shape function S_E in equation (2), is a close approximation of the electric field between the narrow side of two oppositely charged plates. This approximation was made, from the results from a separate electrostatic simulation of a pair of such plates. The electric field between the flat electrodes was calculated assuming an electrode separation of 20 mm, by solving the Poisson equation without any volume charge. The obtained field distribution was approximated with the above expression (2). We choose to simulate flat plates, because this closely matches our experimental device, where the discharge is created between the narrow side of flat diverging electrodes.

Similarly, the spatial distribution, and maximum value of the magnetic flux density, were found from another magnetostatic simulation, where we simulated a pair of permanent magnets with properties identical to those of the real magnets used

in our experimental setup. The magnetic flux density component B_x is taken to be constant in time, and is restricted in a similar way to \mathbf{E} , by introducing a spatial distribution in the form:

$$B_x(y) = 0.6 \text{ (T)} \exp \left[-\frac{1}{2} \frac{y^2}{(8 \text{ (mm)})^2} \right]. \quad (3)$$

2.2. Plasma equations

The plasma species considered in our model are the following: Argon atoms Ar , Argon ions Ar^+ (ionization energy 15.76 eV), Argon molecular ions Ar_2^+ (ionization energy 14.5 eV), and excited atoms for the atomic level $Ar(4s)$ (energy loss 11.65 eV), combining all $4s$ levels as a single lumped excitation level.

2.2.1. Species densities The densities n_s for species s , are calculated using the particle conservation (a.k.a. continuity) equation:

$$\begin{aligned} \frac{\partial n_s}{\partial t} + \nabla \cdot [n_s(\mathbf{u}_s + \mathbf{u}_g)] &= \\ = \frac{\partial n_s}{\partial t} + \nabla \cdot \mathbf{\Gamma}_s + \nabla \cdot (n_s \mathbf{u}_g) &= R_s. \end{aligned} \quad (4)$$

Here \mathbf{u}_s is the average velocity for species s :

$$\mathbf{u}_s = \langle \mathbf{v}_s \rangle = \int_{(\mathbf{v}_s)} \mathbf{v}_s f(v_s) d\mathbf{v}_s,$$

and \mathbf{u}_g is the gas velocity. The source term R_s is the sum of all reaction rates for s .

In our model, the density flux (with respect to gas velocity) $\mathbf{\Gamma}_s = n_s \mathbf{u}_s$ is defined using the so-called drift-diffusion approximation as:

$$\mathbf{\Gamma}_s = \begin{cases} \frac{q_s}{|q_s|} n_s \hat{\mu}_s \mathbf{E} - \hat{\mathbf{D}}_s \nabla n_s, & \text{for charges} \\ -\hat{\mathbf{D}} \nabla n_s = -D_{s,0} \nabla n_s, & \text{for neutrals} \end{cases} \quad (5)$$

where $\hat{\mu}_s$ and $\hat{\mathbf{D}}_s$ are the mobility and diffusion tensors respectively. These tensors are of the form:

$$\hat{\mu}_s = \mu_{s,0} \hat{\mathbf{A}}, \quad \hat{\mathbf{D}}_s = D_{s,0} \hat{\mathbf{A}},$$

where $\mu_{s,0}$ is the isotropic mobility for species s , $D_{s,0}$ is the isotropic diffusion, and $\hat{\mathbf{A}}$ is defined as:

$$\hat{\mathbf{A}} = \begin{bmatrix} 1 & 0 & 0 \\ 0 & 1 & \frac{\omega_{c,s}}{\bar{\nu}_{m,s}} \\ 0 & -\frac{\omega_{c,s}}{\bar{\nu}_{m,s}} & 1 \end{bmatrix}. \quad (6)$$

The tensor $\hat{\mathbf{A}}$ describes the conditions at high neutral density, where the momentum transfer frequency $\bar{\nu}_{m,s}$ is much greater than the gyrofrequency $\bar{\nu}_{m,s} \gg \omega_{c,s}$.

Appendix B presents how the components of $\hat{\mathbf{A}}$ are derived in more detail. All considered reaction rate coefficients (forming the R_s term in equation (4)) and all transport coefficients ($\mu_{s,0}$, $D_{s,0}$) are presented in Appendix A.

Using equation (4), we compute the densities of almost all species, including electrons, ions Ar^+ and excited atoms $Ar(4s)$. Only the densities of the non-excited atoms Ar and the molecular ions Ar_2^+ are computed differently, as shown in equations (7) and (8).

Atomic density equation The gas density n_{Ar} is computed directly from the ideal gas law, as:

$$n_{Ar} = \frac{p}{k_B T_g}, \quad (7)$$

where T_g is the gas temperature, p is the gas pressure, and k_B is the Boltzmann constant. This is valid, because in our problem formulation, we have a small degree of ionization $\sim 10^{-5}$, i.e. the density of the neutrals is much higher than the densities of any of the charge species. In general, the pressure variation in the domain is very small for all conditions considered here.

Quasi-neutrality constraint The quasi-neutrality for plasma is valid for lengths larger than several times the characteristic Debye length and for regions outside the wall sheets. Our model considers atmospheric gas pressure and a cross section of the positive column of the arc. In our finite element implementation of the model, the minimal size of the elements is in the range of tens of micrometers and this size remains orders of magnitude larger than the Debye length. These considerations allow us to apply the quasi-neutrality constraint $n_e = n_{Ar+} + n_{Ar_2^+}$ at every point of the domain Ω , thereby reducing the number of density equations (in the form of equation (4)) for the charged species to only two. For example, in our case the density $n_{Ar_2^+}$ is calculated simply as:

$$n_{Ar_2^+} = n_e - n_{Ar+}, \quad (8)$$

and we solve equation (4), only for n_e and n_{Ar+} and $n_{Ar(4s)}$.

2.2.2. Electron energy balance equation The electron energy balance equation describes the change in energy for the most energetic species – the electrons. In our model it is expressed as:

$$\begin{aligned} \frac{\partial n_e \langle \varepsilon_e \rangle}{\partial t} + \nabla \cdot \mathbf{\Gamma}_{\varepsilon, e} + \nabla \cdot (\mathbf{u}_g n_e \langle \varepsilon_e \rangle) = \\ = -n_e \mathbf{u}_e \cdot \mathbf{E} + n_e \langle \Delta \varepsilon_e \rangle + Q_{bg}, \end{aligned} \quad (9)$$

where $\langle \Delta \varepsilon_e \rangle$ represents the electron energy losses in the different collision events, and $\mathbf{\Gamma}_{\varepsilon, e}$ is the electron energy flux:

$$\mathbf{\Gamma}_{\varepsilon, e} = \hat{\mu}_{\varepsilon, e} n_e \langle \varepsilon_e \rangle \mathbf{E} - \hat{\mathbf{D}}_{\varepsilon, e} \nabla n_e \langle \varepsilon_e \rangle,$$

where $\hat{\mathbf{D}}_{\varepsilon, e} = D_{\varepsilon_e, 0} \hat{\mathbf{A}}$ is the electron energy diffusion tensor and $\hat{\mu}_{\varepsilon, e} = \mu_{\varepsilon_e, 0} \hat{\mathbf{A}}$ is the electron energy mobility tensor. The tensor $\hat{\mathbf{A}}$ was previously defined in equation (6). The values for $\mu_{\varepsilon_e, 0}$ are computed using the BOLSIG+ software [25] and the diffusion coefficient values are found from the relation $D_{\varepsilon_e, 0} = \frac{2}{3} \mu_{\varepsilon_e, 0} \langle \varepsilon_e \rangle$, which is valid at our conditions.

There is a certain low background power density imposed, in the entire simulation domain, hence the inclusion of the Q_{bg} term in equation (9). This artificial heat term, in combination with other artificial density sources, added to the source terms in equation (4), ensures the presence of a background low density plasma. The background plasma, produced by these artificial sources, has a density at least five orders of magnitude lower than the density of the arc region, so there is no effect on the obtained results. Maintaining a background plasma density, reduces the gradients in the variables between the arc and the background and thus decreases the requirements on the discretization grid density.

2.3. Current density conservation equation

In addition to the quasi-neutrality condition $\rho(\mathbf{r}) = 0, \mathbf{r} \in \Omega$, we add the current conservation equation:

$$\nabla \cdot \mathbf{J} = -\frac{\partial \rho}{\partial t} = 0. \quad (10)$$

This adds a constraint for the potential V and correspondingly to the field \mathbf{E} , in the domain plane Ω . Equation (10) ensures that the charge density remains constant and equal to zero $\rho(\mathbf{r}) = 0 = \text{const}$. In our case, we have:

$$\begin{aligned} \nabla \cdot \mathbf{J} &= \nabla \cdot [e\mathbf{\Gamma}_{Ar^+} + e\mathbf{\Gamma}_{Ar_2^+} - e\mathbf{\Gamma}_e] = \\ &= \nabla \cdot [-\sigma_p(\nabla V) + \mathbf{J}_{\text{diff}} + \mathbf{J}_{\mathbf{E} \times \mathbf{B}}] = 0, \end{aligned} \quad (11)$$

where $\sigma_p = e[(\mu_{Ar^+} \times n_{Ar^+}) + (\mu_{Ar_2^+} \times n_{Ar_2^+}) + (\mu_e \times n_e)]$ is the plasma conductivity. For clarity, in equation (11), we have decomposed the current density \mathbf{J} into several components: $\mathbf{J}_E = \sigma_p(\nabla V)$ (current density due to the electric field), \mathbf{J}_{diff} (diffusion current) and $\mathbf{J}_{\mathbf{E} \times \mathbf{B}}$ ($\mathbf{E} \times \mathbf{B}$ drift current). This separation will prove useful in section 2.7, where we examine the boundary conditions. The diffusion and magnetic field drift components are defined as:

$$\begin{aligned} \mathbf{J}_{\text{diff}} &= e(D_{Ar^+} \nabla n_{Ar^+} + D_{Ar_2^+} \nabla n_{Ar_2^+} - D_e \nabla n_e), \\ \mathbf{J}_{\mathbf{E} \times \mathbf{B}} &= e(\mu_{Ar^+}^2 + \mu_{Ar_2^+}^2 - \mu_e^2) n_s B_x E_z, \end{aligned}$$

where we note that the only non-zero ($\mathbf{E} \times \mathbf{B}$) component for our configuration is the y -component, equal to $B_x E_z$.

2.4. Gas fluid velocity

As mentioned in section 2.1, the boundary conditions on W_B are set in such a way, so that the gas velocity distribution inside the domain Ω corresponds to a fully developed laminar flow. Inside the domain region, the gas velocity is affected mainly by the plasma arc. The evolution of the gas velocity and pressure fields is computed using the Navier-Stokes equations:

$$\begin{aligned} \nabla \cdot (\rho_g \mathbf{u}_g) &= 0, \\ \rho_g \frac{\partial \mathbf{u}_g}{\partial t} + \rho_g (\mathbf{u}_g \cdot \nabla) \mathbf{u}_g &= \\ &= \nabla \cdot \left[-p \hat{\mathbf{I}} + \eta (\nabla \mathbf{u}_g + (\nabla \mathbf{u}_g)^T) - \frac{2}{3} \eta (\nabla \cdot \mathbf{u}_g) \hat{\mathbf{I}} \right] + \mathbf{F}, \end{aligned} \quad (12)$$

where ρ_g is the gas density, p is the gas scalar pressure, η is the gas viscosity, $\hat{\mathbf{I}}$ is the identity tensor, and \mathbf{F} is a volumetric force term, which has units of Nm^{-3} .

Drag friction force We introduce the neutral-charge friction through the volumetric force \mathbf{F} (from equation (12)). This volumetric friction force describes the momentum transfer between the neutral gas and charged plasma particles. The force \mathbf{F} is defined as:

$$\mathbf{F} = \sum_s \mathbf{F}_s = \sum_s n_s m_{s,g} \nu_{s,g} (\mathbf{u}_s - \mathbf{u}_g) \quad (13)$$

where the summation is over all charged species s (electrons and ions). The $(\mathbf{u}_s - \mathbf{u}_g)$ term is the relative (relative to the gas flow) velocity for species s , \mathbf{u}_s is the average velocity for s , and $m_{s,g}$ and $\nu_{s,g}$ are the reduced mass and the collision frequency for each gas-charge pair. An expression for \mathbf{u}_s can be found as $\mathbf{u}_s = \mathbf{\Gamma}_s n_s^{-1}$ from equation (5) (see also equation (B.8) from Appendix B). For our numerical model, the volumetric friction force \mathbf{F} is expressed as:

$$\begin{aligned} \mathbf{F} = & m_{e,g} \nu_{e,g} (\mathbf{u}_e - \mathbf{u}_g) + m_{Ar^+,g} \nu_{Ar^+,g} (\mathbf{u}_{Ar^+} - \mathbf{u}_g) + \\ & + m_{Ar_2^+,g} \nu_{Ar_2^+,g} (\mathbf{u}_{Ar_2^+} - \mathbf{u}_g). \end{aligned} \quad (14)$$

2.5. Gas thermal balance

The next equation in the system is the gas thermal balance equation:

$$\rho_g C_p \frac{\partial T_g}{\partial t} + \nabla \cdot (-k_g \nabla T_g) + \rho_g C_p (\mathbf{u}_g \cdot \nabla T_g) = Q_g, \quad (15)$$

where we solve for the gas temperature T_g . Here C_p is the gas heat capacity, k_g is the thermal conductivity, and Q_g is the total gas heating source (power density W/m³). In our model Q_g is limited to the plasma induced heating, resulting from the energy transfer by elastic collisions between electrons and neutrals. The Q_g term is written as:

$$Q_g = \frac{3m_e m_{Ar}}{(m_e + m_{Ar})^2} n_e n_{Ar} k_{el} |q_e| (T_e - T_g).$$

In the above expression, the electron and gas temperatures are expressed in eV. The right side represents the electron energy losses due to elastic collisions with rate coefficient k_{el} . In our model, the temperature for all heavy species is considered to be equal to the gas temperature.

2.6. External circuit

One of the main parameters for our model is the total discharge current I . The value of the total current determines the amount of energy introduced to the system and the strength of the magnetic action on the arc as well. By extension, the diameter of the arc channel and the arc contraction are also determined by the current.

In order to control the current supplied to the discharge, we simulate an external current source through a simple circuit model. The circuit is comprised of a resistor R_B , connected in series to the discharge, and a capacitor C_B , connected in parallel to the discharge. The resistor R_B determines the maximum current, supplied by the voltage source V_{src} . The capacitor C_B is added to smooth out any rapid changes in the cathode voltage V_c , thereby improving the overall numerical stability.

As mentioned in section 2.1, the magnitude of the transverse electric field is computed from the cathode potential V_c by the simple relation $E_z = V_c/d_z$, where d_z is the distance between the cathode and the anode. In order to couple the electric field with the circuit current I , the following equation is included in the model:

$$\begin{aligned} V_c = & V_{src} - R_B \left[I(t) + C_B \frac{dV_c(t)}{dt} \right] = \\ = & V_{src} - \\ - & R_B \left[\frac{V_c}{d_z} \int_{(\Omega)} S_E(\mathbf{r}) \sigma_p(\mathbf{r}) d\mathbf{r} + C_B \frac{dV_c(t)}{dt} \right]. \end{aligned} \quad (16)$$

Here σ_p is the plasma conductivity, and $S_E(\mathbf{r})$ is a shape function which determines the spatial profile of the \mathbf{E}_z field. For the exact formulation of S_E , see equation (2).

2.7. Boundary conditions

This section presents the boundary conditions for each of the model equations, presented in section 2. The vector \mathbf{n} will be used to denote the normal vector to the specific boundary under consideration.

The side boundaries of the domain – W_L and W_R , act as idealized walls, fixed at room temperature and with zero influx of particles. The conditions on the bottom and top boundaries – W_B and W_T are set to effectively represent the domain as a section of an extended infinitely long domain. The bottom boundary serves as a gas flow inlet, and the top boundary as an outlet with no backflow.

Species density boundary conditions We enforce a zero normal electric field component $\mathbf{n} \cdot \mathbf{E} = 0$ (\mathbf{n} is normal to the wall) on all boundaries, which means no flux due to the electric drift. Additionally, we set no diffusion flux on the walls. This results in zero density fluxes, for the side walls W_L and W_R , for all species s :

$$\mathbf{n} \cdot (\mathbf{\Gamma}_s + \mathbf{u}_g n_s) = 0. \quad (17)$$

Correspondingly, this also applies to the electron energy flux (again on the side boundaries):

$$\mathbf{n} \cdot (\mathbf{\Gamma}_{\varepsilon,e} + \mathbf{u}_g n_e \langle \varepsilon_e \rangle) = 0. \quad (18)$$

For the top W_T and bottom W_B boundaries, we also have zero \mathbf{E} drift and diffusion fluxes, but the difference here is that we need to account for the anisotropic y -component of the flux due to the $(\mathbf{E} \times \mathbf{B})$ drift. This additional requirement results in the following boundary condition:

$$-\mathbf{n} \cdot \mathbf{\Gamma}_s = -\mathbf{n} \cdot (n_s \mu_{s,0}^2 E_z B_x). \quad (19)$$

For the electron energy balance equation, we have:

$$-\mathbf{n} \cdot \mathbf{\Gamma}_{\varepsilon,e} = -\mathbf{n} \cdot (n_e \langle \varepsilon_e \rangle \mu_{\varepsilon_e,0} \mu_{e,0} E_z B_x) \quad (20)$$

Gas temperature conditions We assign the bottom boundary W_B and the side walls W_L and W_R to be at constant room temperature. The heat flux on the outlet W_T is set to zero:

$$-\mathbf{n} \cdot (k_g \nabla T_g) = 0, \quad (21)$$

where k_g is the thermal conductivity. This choice proves to be convenient, and allows us to simplify the model, without causing any significant effects on the solution. We are able to use this approximation, since the length of the considered domain is sufficiently large and the arc (heat source) is at a large enough distance from the W_T boundary.

Gas velocity conditions At the bottom boundary W_B , we have a parabolic velocity distribution for the gas velocity \mathbf{u}_g , with a maximum gas speed of $u_{g,\max}$ in the center $x = 0$:

$$[\mathbf{u}_g]_y = u_{g,\max} \left[1 - \left(\frac{x}{W_D/2} \right)^2 \right]. \quad (22)$$

Table 1: Boundary conditions used in model equations. Domain boundaries shown on (figure 1a).

Equation	(11)	(4)	(9)	(12)	(15)
Variables	$V, \mathbf{J}_{\text{diff.}}, \mathbf{J}_{\text{E} \times \text{B}}$	$n_e, n_{Ar^+}, n_{Ar_2^+}, n_{Ar(4s)}$	$n_e \langle \varepsilon_e \rangle$	\mathbf{u}_g	T_g
W_L	$-\mathbf{n} \cdot \mathbf{J} = 0$	(17)	(18)	$\mathbf{u}_g = 0$ no-slip boundary	$T_g = 293.15\text{K}$
W_T	(24)	(19)	(20)	(23)	(21)
W_R	$-\mathbf{n} \cdot \mathbf{J} = 0$	(17)	(18)	$\mathbf{u}_g = 0$ no-slip boundary	$T_g = 293.15\text{K}$
W_B	(24), $V = 0$	(19)	(20)	(22)	$T_g = 293.15\text{K}$

This condition effectively makes the domain to appear at the end of a very long domain between two parallel plates with steady laminar gas flow.

On the top boundary W_T , we have a constant pressure restriction:

$$\left[-p\hat{\mathbf{I}} + \eta (\nabla \mathbf{u}_g + (\nabla \mathbf{u}_g)^T) - \frac{2}{3}\eta (\nabla \cdot \mathbf{u}_g)\hat{\mathbf{I}} \right] = -p_0 \mathbf{n}, \quad (23)$$

where $p_0 = 1 \text{ atm} = 101 \text{ kPa}$. There is an additional backflow suppression as well. Here, ρ_g is the gas density, p is the gas scalar pressure, η is the gas dynamic viscosity and $\hat{\mathbf{I}}$ is the identity tensor. In our model, the viscosity η is a function of temperature and is fed from tabulated data at runtime.

Current conservation equation For the bottom and top boundaries, we set the current density flux to equal only the flux of the $(\mathbf{E} \times \mathbf{B})$ drift component of the current:

$$-\mathbf{n} \cdot \mathbf{J} = -\mathbf{n} \cdot \mathbf{J}_{\text{E} \times \text{B}}. \quad (24)$$

Following equation (11), this means that $-\mathbf{n} \cdot \mathbf{J}_{\text{diff}} = 0$ and $-\mathbf{n} \cdot \sigma_p \nabla V = \mathbf{n} \cdot \sigma_p \mathbf{E} = 0$. These restrictions are coupled with those on the particle density fluxes, discussed earlier. At the bottom boundary W_B , we fix the potential value $V = 0$, setting that wall to be at the reference potential for the domain Ω .

All the boundary conditions are systematized in table 1. The numbers in the table are equation references from this and other sections of the article. The first table row shows the reference number of the examined differential equation. The second row shows the variables of interest for the particular equation. The next four rows show the conditions at each of the domain boundaries.

3. Results and discussion

The previously described mathematical model was implemented into the Comsol Multiphysics $\text{\textcircled{R}}$ (version 5.3) software. The created program was used to compute the solution in time for several distinct simulation configuration.

All simulation runs had identical values for some of the parameters. These are: domain height $H_D = 60 \text{ mm}$, voltage of voltage source $V_{\text{src}} = 5 \text{ kV}$ (see section 2.6), parallel capacitor $C_B = 10 \text{ pF}$, inter electrode distance $d_z = 20 \text{ mm}$. The distribution of the magnetic field in the domain Ω is the same for all runs. It is defined in equation (3), and has a maximum value of 0.6 T at $y = 0$.

Table 2: Values for input simulation parameters.

W_D (mm)	R_B (k Ω)	I (mA)	$u_{y,\text{inlet}}$ interval for a stabilized arc (m/s)
2	50	≈ 100	1-1.4
2	25	≈ 200	1-2
2	12.5	≈ 400	1-2.4
4	50	≈ 100	1-7
4	25	≈ 200	1-7
4	12.5	≈ 400	1-7
20	50	≈ 100	1
20	50	≈ 100	2
20	50	≈ 100	4
20	25	≈ 200	1
20	25	≈ 200	2
20	25	≈ 200	4
20	12.5	≈ 400	1
20	12.5	≈ 400	2
20	12.5	≈ 400	4

Each simulation has a unique set of three input parameters. These are: the domain width W_D , resistance R_B (which limits the maximum circuit current I) and the maximum gas flow velocity on the W_B boundary – $u_{y,\text{inlet}}$. The values of the input parameters for the separate runs are presented in table 2.

If the gas friction drag force acting on the arc is greater than the maximum $I \times B$ force, the plasma arc moves beyond the region where the magnetic field is strong. The effect of the drag force on the arc is mainly determined by the gas flow velocity and the contact area. We consider the arc to be "stabilized", if it remains in the magnetic region for long enough (over 1 s in physical time), and "not stabilized" if it gets pushed by the gas flow beyond the region of strong magnetic field.

A magnetically stabilized arc was observed for a certain interval of gas velocities, in all performed simulations. For the cases with larger wall-to-wall distance (≥ 4 mm), we observed a stabilized arc for flow velocities as high as 7 m/s. In contrast, for those simulations, where the inter-wall distance is small (2 mm), the arc is stabilized only for velocities lower than 2 m/s. Table 2 presents the conditions for all performed simulations, and also the inlet velocity intervals at which the arc remains magnetically stabilized. Considering the available simulation data, we cannot say whether the discharge arc will become stabilized for gas velocities larger than 7 m/s.

It is important to note that, the values of I presented in table 2 are those of the total current, after the arc channel is initialized, and the cathode voltage is steady.

3.1. Quantities of interest

Here we present the definitions of several quantities, which are referred in the presented results, in the next sections.

First, we will define the domain subregion Ω' as the subarea of Ω , where the electron density n_e is at least 10^{17} m^{-3} . This subregion is useful for defining properties related to the arc.

The list of quantities under consideration is the following:

- $n_{e,\max} = \max_{\Omega}(n_e)$ (m^{-3}): The maximum electron density in the domain Ω .
- $\langle T_g \rangle$ (K): The average temperature of the neutral gas in the domain Ω .
- r_{arc} (m): Effective arc radius. Defined from the equation:

$$\max_{\Omega}(n_e)\pi r_{\text{arc}}^2 = \int_{\Omega'} n_e d\Omega' \quad (25)$$

or as the radius of the cylinder, with height $\max_{\Omega}(n_e)$, that has a volume which can enclose the net electron charge in the arc subregion Ω' .

- $F_{\text{D,arc}}$ (N/m): Gas drag force, experienced by the arc, defined per unit length. For a solid cylindrical body, placed in a flowing fluid, the drag force per unit length F_{D} (N/m) is defined as (equation 3.3 from [26]):

$$F_{\text{D}} = \frac{1}{2}C_{\text{D}}\rho_{\text{g}}U^2d, \quad (26)$$

where d is the cylinder diameter, C_{D} is the drag coefficient, ρ_{g} is the gas density and U is the free stream flow velocity (unperturbed velocity in front of the body). For our problem, the arc cannot be represented as a solid, so we choose to define the drag force $F_{\text{D,arc}}$ (N/m) as the integral of the volumetric drag force \mathbf{F} (N/m^3) (see equation (13)), over the arc area Ω' :

$$F_{\text{D,arc}} = - \int_{\Omega'} \mathbf{F} d\Omega', \quad (27)$$

- C_{D} : Drag coefficient. This is the effective drag coefficient for the arc, defined using the relation (26), with $F_{\text{D}} = F_{\text{D,arc}}$ (defined in equation (27)). This gives us:

$$C_{\text{D}} = F_{\text{D,arc}}/(\rho_{\text{g}}\mathbf{u}_{y,\text{inlet}}^2 r_{\text{arc}}). \quad (28)$$

where $\mathbf{u}_{y,\text{inlet}}$ is the y -component of the maximum inlet gas speed, r_{arc} is the effective arc radius and ρ_{g} is the gas density.

- \mathbf{x}_{arc} and \mathbf{y}_{arc} : Arc position. Defined as the position of the point with maximum electron density $\max_{\Omega}(n_e)$.

Before moving to the discussion on the results, we would like to comment shortly on the coupling charged species (plasma) - neutral gas, for the conditions considered here. Obviously the Lorentz force acts on charges having certain velocity and results in the $\mathbf{I} \times \mathbf{B}$ force, i.e. the force is applied to the ions and electrons which determine the current. In our configuration (figure 1), this corresponds to force acting downwards, i.e. upstream. Due to the large mobility of electrons and thus larger electron current and velocity, the force mainly acts on the electrons and much more work is done for the displacement of the electrons. The electron displacement leaves uncompensated positive ions and thus an electric field along the Lorentz force is induced (in our configuration this is the E_y component), which is pulling the ions after the electrons and thus the charged species move together coupled by the electric field and with a velocity, mainly determined by the ion mobility. With respect to the background neutral gas, both ions and electrons contribute to the friction force (equation (13)). Because of the small mass of the electrons, they do not transfer significant momentum and the momentum is transferred to the gas mainly by the ion-neutral collisions. In this way, the Lorentz force is coupled to the gas.

3.2. Arc behaviour at different distances between the side walls

In this subsection we present the typical behavior of the discharge for the different values of the domain width W_D (side wall distance). This parameter causes the most significant change in the arc behavior. It affects the arc size, arc location and others.

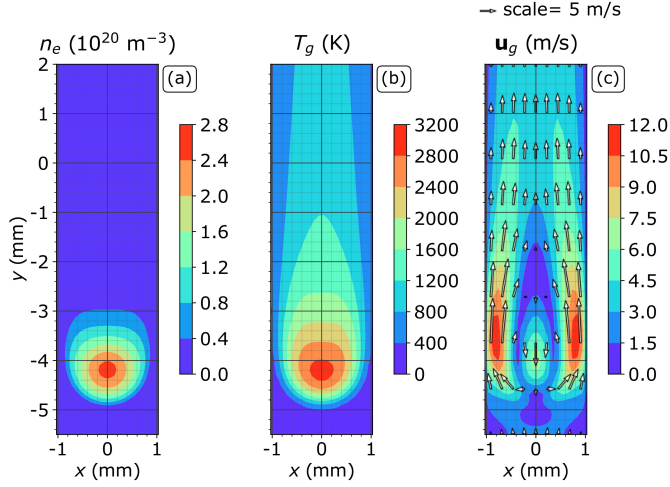


Figure 2: Surface plots of a stabilized state for the $W_D = 2$ mm, $I = 200$ mA case, at an inlet velocity of $\mathbf{u}_{y,\text{inlet}} = 2$ m/s: (a) electron density n_e ; (b) gas temperature T_g ; (c) gas velocity magnitude (color) and vector field (arrows). The arrow scale is given above the figure.

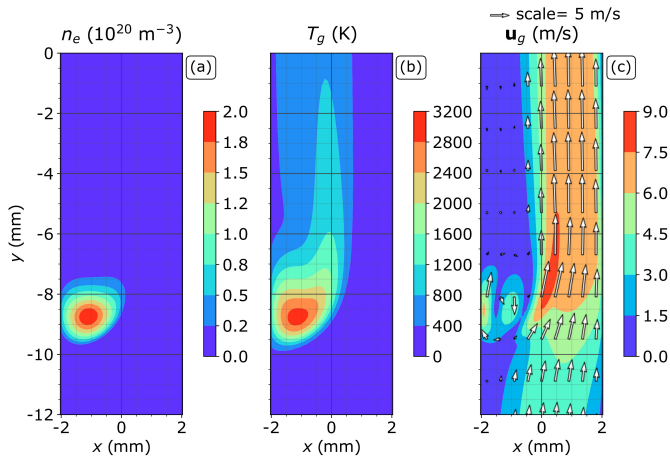


Figure 3: Surface plots of a stabilized state for the $W_D = 4$ mm, $I = 200$ mA case, at an inlet velocity of $\mathbf{u}_{y,\text{inlet}} = 4$ m/s: (a) electron density n_e ; (b) gas temperature T_g ; (c) gas velocity magnitude (color) and vector field (arrows). The arrow scale is given above the figure.

In figures 2 and 3, we see the spatial distribution of the quantities of most interest, i.e. the gas temperature, electron density and gas flow velocity. We can see a clear difference in the arc behavior, between the cases of $W_D = 2$ mm and $W_D = 4$ mm. Both cases have an identical current of $I = 200$ mA, and in both cases a stabilized arc is achieved.

For the small wall distance $W_D = 2$ mm, the arc is localized in the center of the domain region, with two symmetrical flow channels present on both sides. The arc is restricted from any side-to-side (x -directed) motion, mainly because of the small distance between the side walls. The arc radius is comparable to the side wall distance, and the gas cooling from the walls determines the gas temperature profile and thus the arc position. In the literature this is usually referred as a wall stabilized arc.

For the wider side wall distance ($W_D = 4$ mm), the arc is apparently no longer restricted by the channel size, and is able to move sideways. This is because of the smaller arc-to-channel width ratio, compared to the 2 mm simulations. The supplied power is identical for both widths, the arc has an effective radius similar to the 2 mm case, but for $W_D = 4$ mm, the channel is wider.

The arc is initially created in the exact middle of the domain region, on the vertical of maximum gas velocity, but due to the parabolic profile of the gas velocity field (having a maximum in the middle $x = 0$ mm), this initial state is unstable, and the arc tends to move to one side as soon as any small disturbance occurs. In our understanding, any asymmetry or deviation from symmetry in the solution, causes the arc to move either left or right, to the region of smaller flow velocity. In the real world case, we argue that a similar effect can be caused by any small turbulence or asymmetry in the setup or in the gas flow. This initial offsetting causes the flow channel, either on the left or the right side of arc, to become wider as time progresses. As the arc moves to one side, it experiences less drag on the side closer to the nearest side wall. Eventually, the higher gas speed in the wider flow channel, drives the arc close to one of the side walls, and keeps it "pressed" there.

In general, the attachment of the arc to the walls provides a configuration with lower pressure drop in the domain, compared to the case with arc at the center. Moreover this is related to a lower friction force applied to the arc from the gas flow when the arc is near the walls since at that position the arc is in region with lower gas velocity.

Although we are not ready to reveal any extensive experimental results in this study, we will mention that during our laboratory tests, we repeatedly observed this kind of arc behavior, with the arc column "sticking" to one of the vessel walls. These tests were done in similar conditions – closely matching configuration, with a side wall distance of 4 mm, at similar gas flow and magnetic flux densities.

Figures 4, 5 and 6, present the case for large wall-to-wall distances $W_D = 20$ mm, with slip boundary condition and no heat flux at the walls. The wider 20 mm configurations provide a way to exclude the effect of the side walls. One can think of these simulations, as having infinite domain width and constant velocity along the x axis.

The results computed for the large 20 mm width, show a behavior very different than that in the case of the small channel widths (2 mm and 4 mm). The arc remains localized in the center of the domain, with an observable periodic motion in the x -direction.

Figure 4 shows the electron density n_e distribution at different moments in time, for one period ($T \approx 6$ ms) of the periodic motion. Figures 5 and 6 present how the

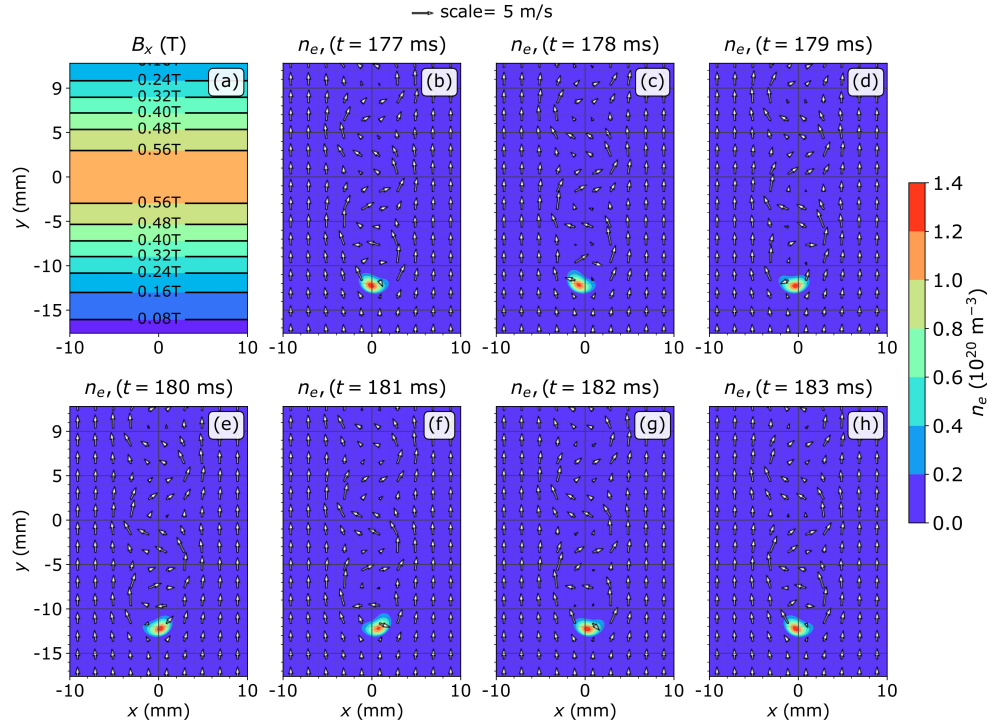


Figure 4: Spatial distribution of the electron density n_e for one period of arc oscillation. The examined case is for $W_D = 20$ mm (infinite wall distance), at $I = 200$ mA and inlet velocity of 2 m/s. Subfigure (a) shows the spatial distribution of the magnetic flux density. The arrows show the gas velocity field, with the arrow scale given above the figure. A better visualization of the arc motion is available as a video, in the supplementary files to this article.

distribution of the electron density and the gas temperature change, as the gas velocity is increased. They clearly show that the frequency of this oscillation increases with the gas flow velocity. This effect is examined in more detail in the next subsection 3.3. We can also see that the arc has a higher y position, i.e. it is stabilized at higher magnetic field, as the gas inlet velocity increases. This is due to the increased drag experienced by the arc, requiring higher magnetic force (field) in order to be compensated.

Another observable feature is the vortex shedding, formed in the arc's wake. Apparently the arc motion and the vortex dynamics are closely coupled. In general, the formation of vortices in a cross flow configuration, with a bluff body, is related to flow separation and the formation of a low pressure zone just after the body (downstream). The vortices behind the body become unstable if the Reynolds number is sufficiently high - in the order of 50 and higher, and a vortex street (also known as a Kármán vortex street) is formed [17].

Here, in our configuration, the motion is more complicated due to the arc being part of the gas. The gas comprising the arc is under additional volume forces and

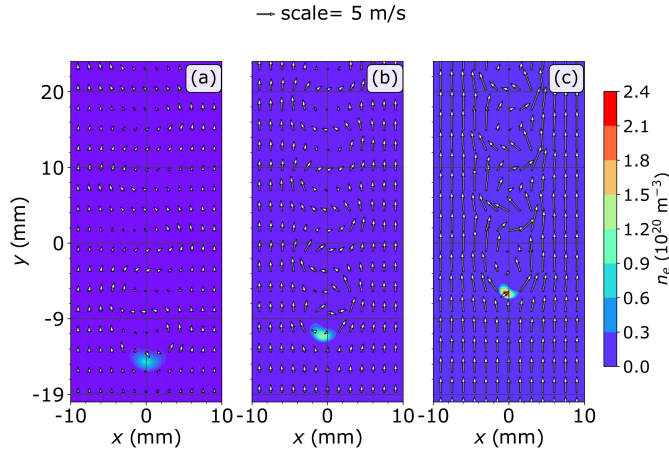


Figure 5: Comparing the spatial electron density distribution n_e for the case with a large inter-wall distance $W_D = 20$ mm (infinite wall distance), at $I = 200$ mA, for different gas flow velocities: (a) $\mathbf{u}_{y,\text{inlet}} = 0.95$ m/s; (b) $\mathbf{u}_{y,\text{inlet}} = 1.97$ m/s; (c) $\mathbf{u}_{y,\text{inlet}} = 4$ m/s; The arrows show the gas velocity field, with the arrow scale given above the figure.

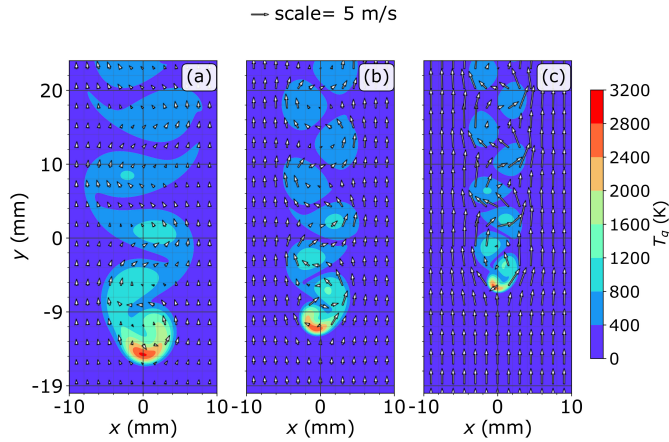


Figure 6: Comparing the spatial gas temperature distribution T_g for the case with a large inter-wall distance $W_D = 20$ mm (infinite wall distance), at $I = 200$ mA, for different gas flow velocities: (a) $\mathbf{u}_{y,\text{inlet}} = 0.95$ m/s; (b) $\mathbf{u}_{y,\text{inlet}} = 1.97$ m/s; (c) $\mathbf{u}_{y,\text{inlet}} = 4$ m/s; The arrows show the gas velocity field, with the arrow scale given above the figure.

the arc does not have well defined boundaries, shape and position. The vortex shedding causes the arc to move towards the lower pressure regions, which results in the oscillating pattern observed in figure 4. In the literature this kind of instability is referred as flutter instability [17].

Figure 7 shows the arc path for different gas velocities and fixed current. The path

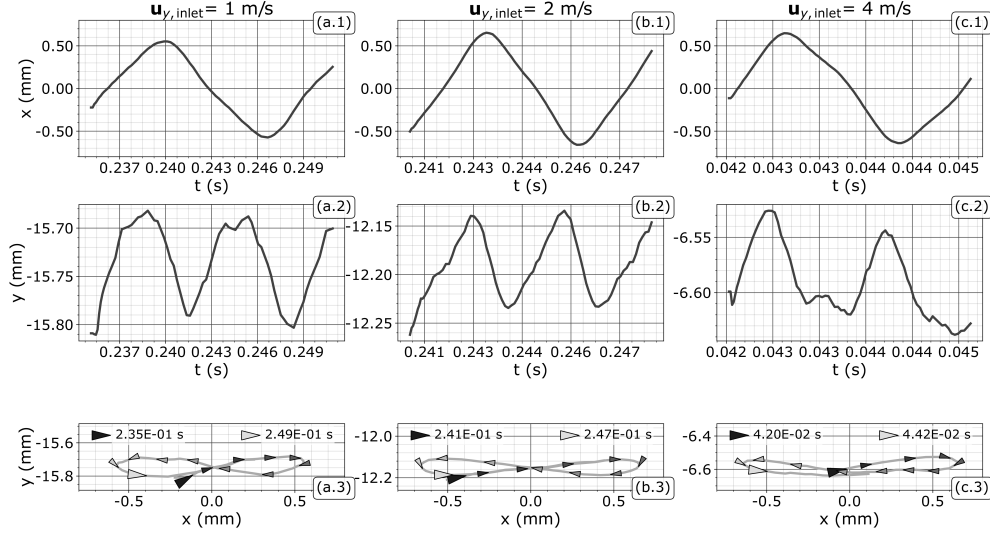


Figure 7: Arc motion path for the cases with $W_D = 20$ mm, $I = 200$ mA: (a) $u_{y,\text{inlet}} = 1$ m/s, x -oscillation period $T \approx 12$ ms; (b) $u_{y,\text{inlet}} = 2$ m/s, x -oscillation period $T \approx 6$ ms; (c) $u_{y,\text{inlet}} = 4$ m/s, x -oscillation period $T \approx 3$ ms; The position of the arc is taken to be the point with the maximum electron density n_e .

is shaped as the "8" digit with a very small oscillation amplitude in the y -direction. Note that the figures with the paths (figure 7 a.3 to c.3) are shown with equal scaling along the x and y axes. The direction of motion is also shown. The frequency of the oscillation in y -direction is twice the frequency in x -direction which results in the eight-shaped path.

An interesting observation worth mentioning is that the arc always goes upward (in the y -direction), when it is close to the turning point (in the center), and goes down, when it is in the peak of the x -oscillation. The data shows that this effect is related to the periodic variation of the maximum gas temperature. The maximum value of the gas temperature occurs at the turning point, when the arc is located in the center of the domain region. At that stage, the arc is moving with the gas flow in y -direction. When the arc is at its peak position in x , the gas temperature has a minimum and arc is moving downwards (upstream), i.e. against the gas flow in the y -direction. We attribute this relation to the difference in the convective cooling due to the lower relative velocity of the arc with respect to gas in the first case (the center) and thus lower heat transfer, and to the higher relative velocity with respect to the gas and thus higher heat transfer in the second case.

3.3. Quantities as a function of gas velocity

This section presents the relations between the gas velocity at the inlet – $u_{y,\text{inlet}}$ and the main macroscopic quantities. Figures 8 and 9, show how the oscillation frequency in the 20 mm case changes with the gas velocity. The average gas temperature $\langle T_g \rangle$, the maximum electron density $n_{e,\text{max}}$, the effective arc radius r_{arc} (see section 3.1 for definitions) and others, are shown on figures 10 and 11. Additionally, on figures 12 and 13, we present a rough estimate for the drag force F_D and drag coefficient

C_D , for the examined discharge configuration. The analysis of the relations of these quantities to the gas flow and current is critical to the understanding of the processes in the plasma and to the potential improvement of the gas treatment efficiency in real conditions. For some processes of interest to us, namely the dissociation of CO_2 , the main factors which directly determine the efficiency are the gas temperature, the electron temperature and electron density. Looking at the current research in the area of CO_2 treatment [1, 2], these quantities determine the densities of the excited molecular vibrational levels. This is important, because for a vibrationally excited molecule, the threshold for dissociation is lowered.

The plotted data for the $W_D = 20$ mm simulations is found, by averaging the quantities of interest over several periods of the x -directed oscillation.

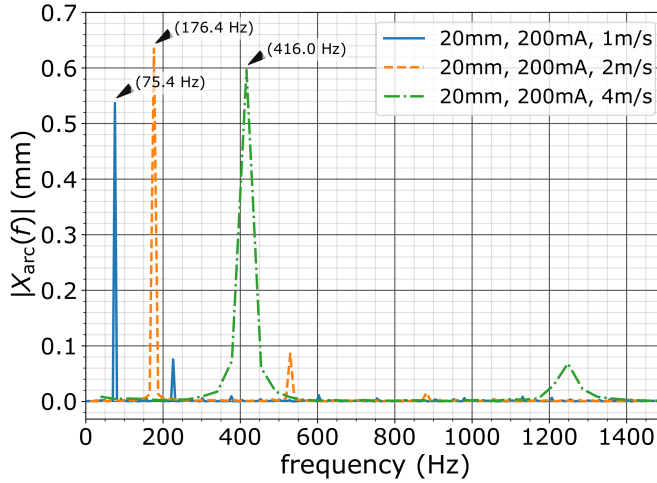


Figure 8: Amplitude spectrum lines for the x -oriented arc oscillations, in the case of $W_D = 20$ mm, $I = 200$ mA.

Figures 8 and 9 show an increase in the x -directed oscillation frequency, as a result of the increase in the gas flow velocity. This was mentioned in the comment for figures 5 and 6. Again, looking at those figures, we can observe how the shedding phenomenon is more developed in the cases of higher gas flow speed. The increase in frequency follows the Strouhal relation for vortex shedding (formula 3.2 of [17]):

$$f_s = \frac{SU}{d}, \quad (29)$$

where the shedding frequency f_s is proportional to the free stream flow velocity U (corresponding to $\mathbf{u}_{y,\text{inlet}}$ in our model), and S is the so-called Strouhal number, which is a dimensionless proportionality constant. Equation (29) assumes a solid cylinder with radius d placed in a flowing fluid stream.

In figure 10(a), we can see that the mean gas temperature $\langle T_g \rangle$ (for the entire domain region) decreases with the increase in the inlet gas velocity. We can also observe that $\langle T_g \rangle$ increases with the current, which is expected since the increased current leads to increase in the power as well. It is interesting to note that as the gas flow velocity increases, the maximum gas temperature (not shown here) remains fairly constant, even if we increase the total power. This effect could be the result of increased cooling, caused by the larger gas flow.

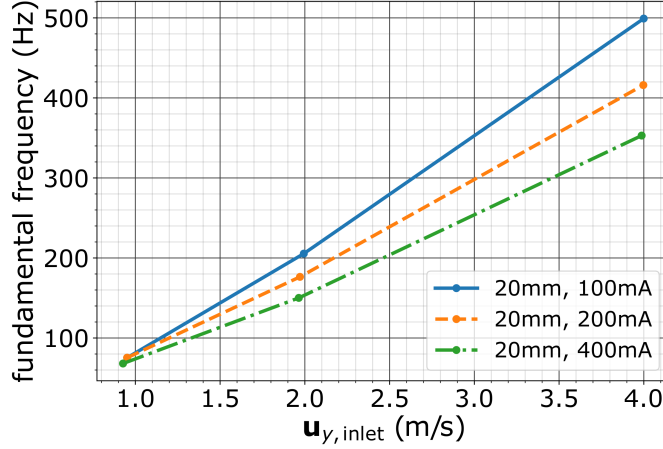


Figure 9: Fundamental x -oscillation frequencies as a function of the gas flow velocity, for all 20 mm configurations.

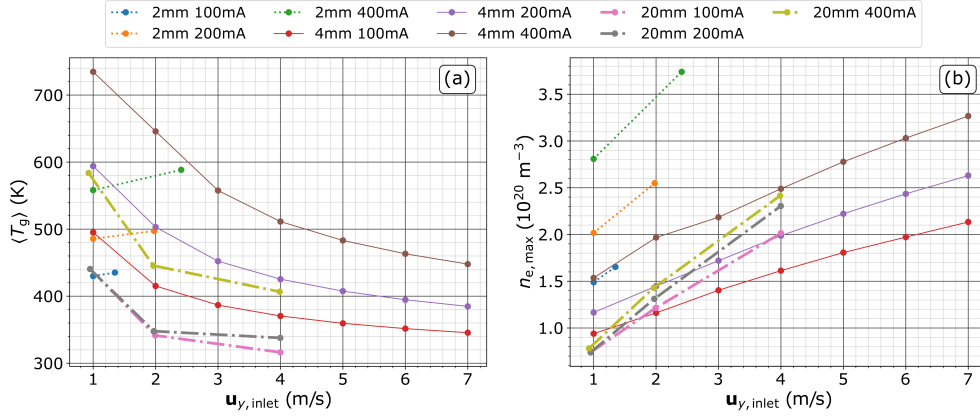


Figure 10: The mean gas temperature $\langle T_g \rangle$ (a) and the maximum electron density $n_{e,\text{max}}$ (b) as a function of the inlet gas flow velocity $u_{y,\text{inlet}}$.

From figure 10(b), we see that $n_{e,\text{max}}$ has the tendency to increase with the gas velocity, but only slightly. The maximum electron density also increases with the current which is expected, but also by a very small amount.

On figure 12(a), we can observe that the arc radius r_{arc} decreases with the gas velocity, but at the same time increases with the current. We argue that the decrease with the inlet flow is related to the effect of arc contraction. At the same time, the maximum electron density and corresponding maximum current density remain fairly constant, as noted previously. This explains the increase in the effective arc radius with larger currents. If the maximum current density remains practically constant, which is the case, larger net current will result in larger arc area, and therefore bigger arc radius. Note also that the arc contraction and gas cooling are strongly affected by the gas flow, which in turn is affected by the arc itself.

Figure 11(a) shows the y position of arc stabilization (averaged over one period

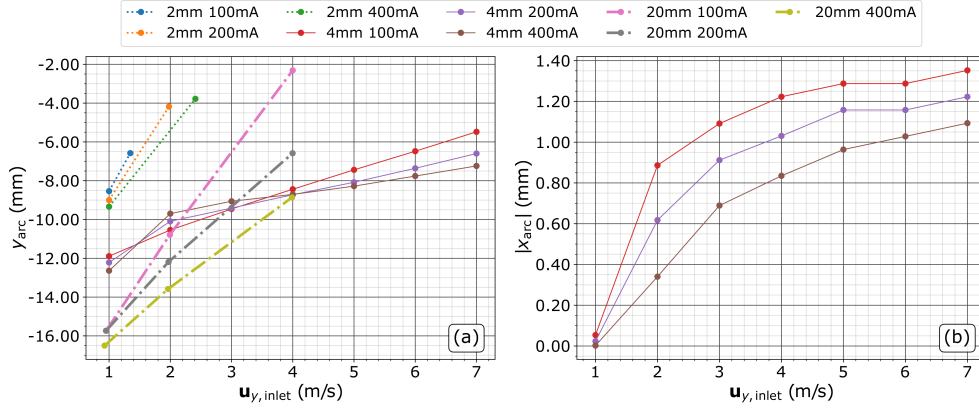


Figure 11: Arc position as a function of the inlet gas flow velocity $u_{y,\text{inlet}}$: y component y_{arc} (a); absolute value of x component x_{arc} (b), (the walls are at $x = 2$ mm).

for the 20 mm cases). Clearly the higher gas velocity pushes the arc downstream (upwards in the y -direction), due to the increased friction. Apparently the strongest friction with the gas is observed for the shortest wall distance $W_D = 2$ mm. This determines the highest values for the effective drag coefficient C_D , shown in figure 12(b). For the 4 mm case, we see a fairly weak influence of the gas velocity on the y_{arc} position. This is probably related to the arc radius and the arc distance from the wall, shown in figure 11(b). As the gas velocity increases, the arc is pushed closer to the wall (figure 11(b)) and it is getting tinier (figure 12(a)). Thus, the arc is subject to gas velocity lower compared to the central maximum gas velocity (the gas velocity becomes zero at the wall).

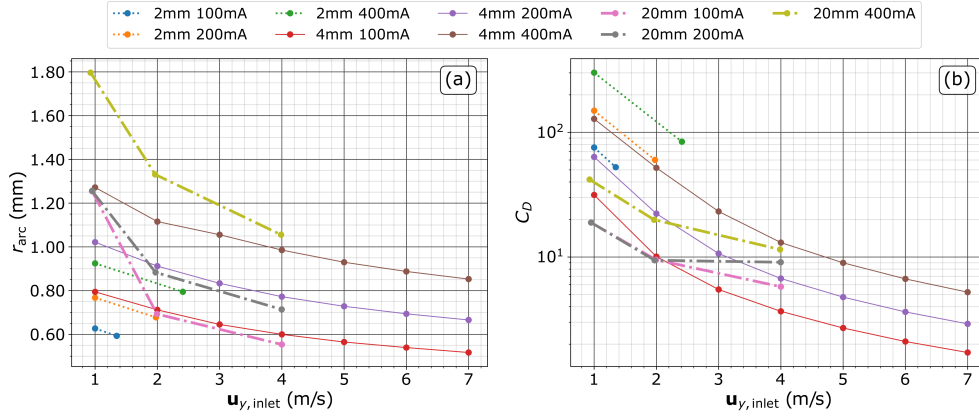


Figure 12: The effective arc radius r_{arc} (a) and the effective drag coefficient C_D (b) as a function of the inlet gas flow velocity $u_{y,\text{inlet}}$.

The effective drag coefficient C_D (figure 12(b)) shows a large variation. The most significant values are for the $W_D = 2$ mm cases. There is clearly a decrease of C_D with gas velocity.

We want to stress that the effective coefficient C_D should be taken only as a rough estimation because it is calculated based on a relation valid for solid cylinder while the arc is neither a cylinder or solid. The arc radius is based on the electron density distribution and thus on the current. The gas temperature distribution is generally wider and we should keep in mind that gas viscosity increases with the temperature, which means that the effective radius of the "body", which disturbs the gas flow, could be larger. It should also be noted that the values for C_D presented here generally decrease with the gas velocity, which is similar in nature to the case of a solid cylinder for Reynolds numbers below 1000 [17].

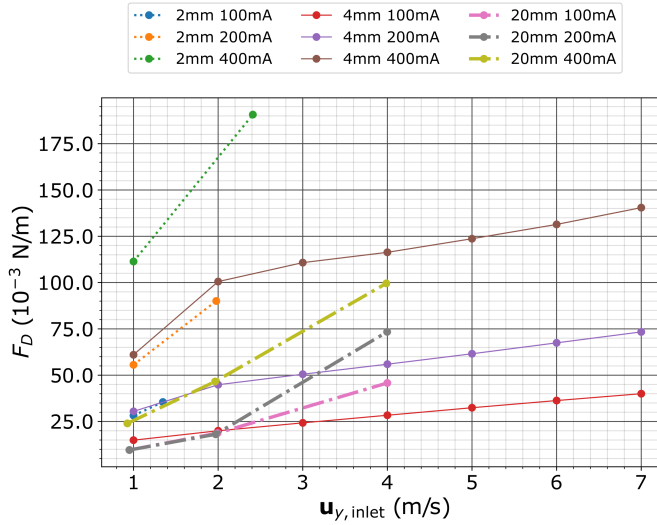


Figure 13: The drag force F_D as a function of the inlet gas flow velocity $u_{y,inlet}$.

For completeness, we also show the drag force F_D (figure 13) used to calculate the effective drag coefficient C_D (figure 12(b)), using the effective arc radius r_{arc} (figure 12(a)). Generally the force is increasing with the gas velocity as expected.

4. Conclusions

We presented the results from numerous computer simulations, which show the interaction of a DC arc under the effect of a Lorentz force and gas flow, in argon at atmospheric pressure.

The results show a very strong influence of the walls on the arc stabilization. The magnetic stabilization of the arc in gas flow presents an unique configuration from fluid dynamics perspective. In contrast to wall stabilization of arcs, the magnetic field force acts on the gas itself through the friction with the charged species and allows for configurations which are not affected of the walls at all. In this study, three distinct types of behavior were observed. 1) When the arc is operating between closely spaced side walls with a distance of approximately two times the arc diameter, the arc is stabilized in the middle between the walls due to the intense cooling from the walls and the gas flow between the arc and the walls, where the gas velocity rises in order to sustain the same overall gas flow imposed on the inlet. 2) When the wall distance

is larger (several arc diameters), the arc tends to attach to one of the walls. This state leads to smaller drag from the gas compared to the middle between the walls, because of the lower gas velocity near the walls and the decreased gas pressure drop as a result of the increased gas flow channel. 3) When the walls are far from the arc and the transverse gas velocity distribution in the arc region is close to homogeneous without arc, the arc becomes a source of vortices and a gas flow instability, producing the well known Kármán vortex street. Since the arc is not fixed at certain position, the vortices lead to vortex induced vibrations of the arc.

With respect to the arc stabilization, the short wall distance case makes the stabilization much harder, i.e. higher magnetic field is needed to stabilize the arc at a given current. This is a result of an increased friction due to the increased gas velocity at the arc edges. The case with larger wall distance allows easier stabilization and the arc is subject to less friction. In the case of the very large wall distance, the arc vibrations become more intense with the rise in gas velocity, which increases the friction with the gas, and reduces the ability of the Lorentz force to stabilize the arc at certain position for given arc current.

With respect to gas treatment, the above mentioned phenomena may prohibit the treatment of gas at high inlet flow velocities. The best configuration in this regard is the second one, where the arc moves to the side. However this configuration allows more gas to pass the discharge untreated.

In parallel to our work on creating computer models, our team is actively involved in the design and development of an experimental gas treatment reactor. This reactor employs the concept of the magnetically stabilized arc discharges, in a similar configuration to the numerical model presented here. The considered design includes the use of a fully stabilized arc by means of strong permanent magnets, providing magnetic field in direction perpendicular to the arc current. At the same time, the gas flow is injected transversely to both the arc and the magnetic field. This type of configuration is of particular interest to us, because it is inexpensive, and has the potential to improve the efficiency of gas treatment of CO₂ and other gases.

By doing actual laboratory tests, using an early reactor prototype, we were able to show the arc stabilization and other effects, similar to those in the simulation results of this study. In particular, we repeatedly observed the arc to "stick" to one of the vessel's side walls, in conditions very similar to those of our computer simulations with $W_D = 4$ mm, in which the same behavior is found. At that stage of the study, the experiment is not capable of providing precise data for quantitative comparison with the presented here numerical results. This will be studied in the near future.

Looking at the promising early results, we consider to further investigate the configuration of a magnetically stabilized DC arc in flowing gas, and the related phenomena. The lack of information about the processes in such systems, especially at low currents, motivates us to develop more detailed numerical models in argon and other gases as well. These studies may further the understanding of arc discharges at these conditions, and help to improve the design of gas treatment reactors in the future.

Acknowledgments

This work was supported by the Bulgarian National Science Fund, Ministry of Education and Science, research grant KP-06-OPR 04/4 from 14.12.2018 and by the European Regional Development Fund within the Operational Programme "Science

Table A1: Electron collisions included in the model.

No.	Reaction	Rate Coefficient	Source
1	$Ar + e^- \rightarrow Ar + e^-$	BOLSIG	[29]
2	$Ar + e^- \rightarrow Ar^+ + 2e^-$	BOLSIG	[29]
3	$Ar(4s) + e^- \rightarrow Ar^+ + 2e^-$	BOLSIG	[30]
4	$e^- + Ar(4s) \rightarrow e^- + Ar$	BOLSIG	[29]
5	$e^- + Ar \rightarrow e^- + Ar(4s)$	BOLSIG	[29]
6	$e^- + Ar \rightarrow e^- + Ar(4d)$	BOLSIG	[29]
7	$Ar^+ + 2e^- \rightarrow Ar + e^-$	$k = (T_e^{-4.5}(\text{eV}))(8.75 \times 10^{-39})$	[31]
8	$Ar^+ + e + Ar \rightarrow Ar + Ar$	$k = (1.5 \times 10^{-40})(T_g(\text{K})/300)^{-2.5}$	[32]
9	$Ar_2^+ + e \rightarrow Ar^+ + Ar + e$	$k = (1.11 \times 10^{-12}) \times A,$ $A = \exp\left[-\frac{2.94-3(T_g(\text{eV})-0.026)}{T_e(\text{eV})}\right]$	[33]
10	$Ar_2^+ + e \rightarrow Ar + Ar(4s)$	$k = 1.04 \times 10^{-12} [300/T_e(\text{K})]^{0.67} \times A,$ $A = \frac{1-\exp[-418/T_g(\text{K})]}{1-0.31 \exp[-418/T_g(\text{K})]}$	[34, 35]

and Education for Smart Growth 2014 - 2020” under the Project CoE ”National center of mechatronics and clean technologies” BG05M2OP001 – 1.001 – 0008 – CO1.

Appendix A. Transport and reaction rate coefficients

Appendix A.1. Transport coefficients

The transport coefficients $\mu_{s,0}$ and $D_{s,0}$ are formulated differently for each plasma species. The electron mobility $\mu_{e,0}$ is calculated using the Boltzmann equation solver – BOLSIG+ [25]. The ionic Ar^+ mobility is defined as in [27]:

$$\mu_{Ar^+} = \frac{1.01 \times 10^5 T_g(\text{K})}{p(\text{Pa})} \frac{1.52 \times 10^{-4} (\text{m}^2\text{V}^{-1}\text{s}^{-1})}{273.16},$$

where p is the gas pressure and T_g is the gas temperature. The mobility of the molecular ions Ar_2^+ , again from [27], is defined simply as $\mu_{Ar_2^+} = 1.2\mu_{Ar^+}$. The electron and ion diffusion coefficients are derived from their corresponding mobilities, using the Einstein relation.

The $Ar(4s)$ diffusion coefficient is defined as (from [28]):

$$D_{Ar(4s)} = \frac{1}{n_{Ar}} 1.16 \times 10^{20} \left(\frac{T_g(\text{K})}{300}\right)^{(1/2)} (\text{m}^2/\text{s}).$$

Appendix A.2. Reaction rate coefficients

In this section we present all reaction rate coefficients considered in our model. The reaction rate values are presented in tables A1, A2, with their corresponding chemical reactions and literature source. The ”BOLSIG” word is found on rows, which contain reactions that have their rate coefficients computed using the BOLSIG+ solver [25].

Table A2: Heavy species collisions included in the model.

No.	Reaction	Rate Coefficient	Source
11	$Ar(4s) + Ar(4s) \rightarrow Ar^+ + Ar + e^-$	$k = 1.62 \times 10^{-16} \times (T_g[\text{K}])^{1/2}$	[36]
12	$Ar(4s) + Ar(4s) \rightarrow Ar_2^+ + e$	$k = (3.15 \times 10^{-16})(T_g/300[\text{K}])^{-1/2}$	[37]
13	$Ar^+ + 2Ar \rightarrow Ar_2^+ + Ar$	$k = (2.5 \times 10^{-43})(T_g/300[\text{K}])^{-3/2}$	[38]
14	$Ar_2^+ + Ar \rightarrow Ar^+ + 2Ar$	$k = \frac{(6.06 \times 10^{-12})}{T_g[\text{K}]} \times A,$ $A = \exp(-1.51 \times 10^4/T_g[\text{K}])$	[33]

Appendix B. Derivation of the mobility and diffusion tensors for magnetized plasma

This section presents a short derivation of the components of the mobility and diffusion tensors, for the conditions of our model, i.e. the case of magnetized plasma at atmospheric pressure. We start from the magnetized form the of drift-diffusion equation (equation 5-20 in [39]):

$$n_s \mathbf{u}_s + \boldsymbol{\Omega}_s \times (n_s \mathbf{u}_s) = \frac{q_s}{|q_s|} \mu_s n_s \mathbf{E} - \nabla(Dn_s) = \mathbf{G}_s. \quad (\text{B.1})$$

This equation is a simplified version of the general momentum equation (equation 5.13 in [39]), in the drift-diffusion approximation, with an additional $\boldsymbol{\Omega}_s \times (n_s \mathbf{u}_s)$ term. The \mathbf{G}_s vector is the magnetized flux, and $\boldsymbol{\Omega}_s$ is the so called magnetization vector, defined as:

$$\boldsymbol{\Omega}_s = \frac{\omega_{c,s}}{\bar{\nu}_{m,s}} = \frac{q_s \mathbf{B}}{m_s \bar{\nu}_{m,s}} = \frac{q_s}{|q_s|} \mu_s \mathbf{B}, \quad (\text{B.2})$$

where $\omega_{c,s}$ is the magnetic gyrofrequency and $\bar{\nu}_{m,s}$ is the macroscopic momentum transfer frequency. The frequency $\bar{\nu}_{m,s}$ contains the sum of individual frequencies $\nu_{s,s'}$, between s and all other species s' . The magnitude of the $\boldsymbol{\Omega}_s$ vector – $|\Omega_s|$ is called a "Hall parameter". The Hall parameter value is greater for the electrons, because of their small mass.

Multiplying equation (B.1) by $(\boldsymbol{\Omega}_s \times)$ yields:

$$\boldsymbol{\Omega}_s \times n_s \mathbf{u}_s + \boldsymbol{\Omega}_s \times (\boldsymbol{\Omega}_s \times n_s \mathbf{u}_s) = \boldsymbol{\Omega}_s \times \mathbf{G}_s. \quad (\text{B.3})$$

If we apply the formula $\mathbf{A} \times (\mathbf{B} \times \mathbf{C}) = \mathbf{B}(\mathbf{A} \cdot \mathbf{C}) - \mathbf{C}(\mathbf{A} \cdot \mathbf{B})$ to the second term in equation (B.3), we get:

$$\boldsymbol{\Omega}_s \times n_s \mathbf{u}_s = \boldsymbol{\Omega}_s \times \mathbf{G}_s + n_s \mathbf{u}_s |\boldsymbol{\Omega}_s|^2 - \boldsymbol{\Omega}_s (\boldsymbol{\Omega}_s \cdot n_s \mathbf{u}_s). \quad (\text{B.4})$$

Further, one can find that the last term $\boldsymbol{\Omega}_s (\boldsymbol{\Omega}_s \cdot n_s \mathbf{u}_s)$ is equal to $\boldsymbol{\Omega}_s (\boldsymbol{\Omega}_s \cdot \mathbf{G}_s)$ by noting that $\boldsymbol{\Omega}_s \cdot (\boldsymbol{\Omega}_s \times n_s \mathbf{u}_s) = 0$. Next, we express the density flux vector $\boldsymbol{\Gamma}_s = n_s \mathbf{u}_s$, using the magnetized flux \mathbf{G}_s , by substituting equation (B.4) in (B.1):

$$\boldsymbol{\Gamma}_s = n_s \mathbf{u}_s = \frac{1}{(1 + |\boldsymbol{\Omega}_s|^2)} [\mathbf{G}_s - \boldsymbol{\Omega}_s \times \mathbf{G}_s + \boldsymbol{\Omega}_s (\boldsymbol{\Omega}_s \cdot \mathbf{G}_s)]. \quad (\text{B.5})$$

As shown in equation (5), our model uses the drift-diffusion approximation for $\boldsymbol{\Gamma}_s$. The density flux $\boldsymbol{\Gamma}_s$, written in terms of the the mobility $\hat{\mu}_s$ and diffusion $\hat{\mathbf{D}}_s$ tensors is:

$$\boldsymbol{\Gamma}_s = \frac{q_s}{|q_s|} \hat{\mu}_s n_s \mathbf{E} - \nabla(\hat{\mathbf{D}} n_s) = \frac{q_s}{|q_s|} (\mu_{s,0} \hat{\mathbf{A}}) n_s \mathbf{E} - \nabla(D_{s,0} \hat{\mathbf{A}}) n_s, \quad (\text{B.6})$$

where $\mu_{s,0}$ is the isotropic mobility and $D_{s,0}$ is the isotropic diffusion coefficients. If we examine the case of our configuration (where $\mathbf{B} = [B_x, 0, 0]$), using the expression in equation (B.5), we can write the tensor $\hat{\mathbf{A}}$ (from (B.6)) as:

$$\hat{\mathbf{A}} = \begin{bmatrix} A_{\parallel} & 0 & 0 \\ 0 & A_{\perp} & A_T \\ 0 & -A_T & A_{\perp} \end{bmatrix}, \quad (\text{B.7})$$

$$A_{\parallel} = 1, \quad A_{\perp} = \frac{\bar{\nu}_{m,s}^2}{\bar{\nu}_{m,s}^2 + \omega_{c,s}^2}, \quad A_T = \frac{\omega_{c,s}\bar{\nu}_{m,s}}{\bar{\nu}_{m,s}^2 + \omega_{c,s}^2}.$$

Here A_{\parallel} is the component parallel to \mathbf{B} , and A_{\perp} , A_T are the tensor components in the plane perpendicular to \mathbf{B} . It is easy to find the expressions for A_{\perp} and A_T , from equation (B.5), noting that $\boldsymbol{\Omega}_s = \omega_{c,s}/\bar{\nu}_{m,s}$. At atmospheric pressure, as in our case, the collision frequency is much larger than the gyrofrequency $\bar{\nu}_{m,s} \gg \omega_{c,s}$, so at those conditions we have $A_{\perp} = 1$ and $A_T = \omega_{c,s}/\bar{\nu}_{m,s} = \boldsymbol{\Omega}_s$. Following this approximation, we can write \mathbf{I}_s in a vector form as:

$$\mathbf{I}_s = \frac{q_s}{|q_s|} n_s \mu_{s,0} \mathbf{E} + \mu_{s,0}^2 n_s (\mathbf{E} \times \mathbf{B}) - \nabla D_{s,0} n_s, \quad (\text{B.8})$$

$$\mu_{s,0} = \frac{e}{m_s \bar{\nu}_{m,s}}, \quad D_{s,0} = \frac{k_B T_s}{m_s \bar{\nu}_{m,s}}.$$

References

- [1] Snoeckx R and Bogaerts A 2017 *Chem. Soc. Rev.* **46**(19) 5805–5863
- [2] Bogaerts A, Berthelot A, Heijkens S, Kolev S, Snoeckx R, Sun S, Trenchev G, Van Laer K and Wang W 2017 *Plasma Sources Sci. Technol.* **26**
- [3] Fridman A 2008 *Plasma Chemistry* (Cambridge University Press)
- [4] Scott E K 1912 *Journal of the Royal Society of Arts* **60**
- [5] Balcon N, Benard N, Braud P, Mizuno A, Touchard G and Moreau E 2008 *J. Phys. D: Appl. Phys.* **41** 205204
- [6] Myers T W and Roman W C 1966 Survey of investigations of electric arc interactions with magnetic and aerodynamic fields Tech. rep. Aerospace Research Laboratories
- [7] Desaulniers-Soucy N and Meunier J L 1995 *J. Phys. D: Appl. Phys.* **28** 2505–2513
- [8] Gangoli S P, Gutsol A F and Fridman A A 2010 *Plasma Sources Sci. Technol.* **19** 065003
- [9] Gangoli S P, Gutsol A F and Fridman A A 2010 *Plasma Sources Sci. Technol.* **19** 065004
- [10] Zhang H, Du C, Wu A, Bo Z, Yan J and Li X 2014 *Int. J. Hydrogen Energy* **39** 12620–12635
- [11] Zhang H, Zhang H, Trenchev G, Li X, Wu Y and Bogaerts A 2020 *Plasma Sources Sci. Technol.* **29** 045019
- [12] Feng Z, Saeki N, Kuroki T, Tahara M and Okubo M 2011 *IEEE Trans. Plasma Sci.* **39** 2846–2847
- [13] Klein J F and Winograd Y Y 1969 *AIAA J.* **7** 1699–1703
- [14] Cowley M D 1967 A boundary layer model for balanced arcs Tech. rep. Fluid Mechanics Lab., Massachusetts Institute of Technology
- [15] Buczek C J, Freiberg R J, Chenausky P P and Wayne R J 1971 *Proc. IEEE* **59** 659–667
- [16] Essiptchouk A M, Sharakhovskiy L I and Marotta A 2000 *J. Phys. D: Appl. Phys.* **33** 2591–2597
- [17] Blevins R D 2001 *Flow induced vibration* (Krieger Publishing company)
- [18] Roman W C and Myers T W 1967 *AIAA J.* **5**
- [19] Kolev S, Sun S R, Trenchev G, Wang W, Wang H and A B 2017 *Plasma Processes Polym.* **14**
- [20] Kolev S and Bogaerts A 2018 *Plasma Sources Sci. Technol.* **27** 125011
- [21] Kolev S and Bogaerts A 2015 *Plasma Sources Sci. Technol.* **24** 065023
- [22] Kolev S and Bogaerts A 2015 *Plasma Sources Sci. Technol.* **24** 015025
- [23] Fridman A, Nester S, A Kennedy L, Saveliev A and Mutaf-Yardimci O 1999 *Prog. Energy Combust. Sci.* **25** 211–231
- [24] Li L, Zhang H, Li X, Huang J, Kong X, Xu R and Tu X 2020 *J. CO2 Util.* **35** 28–37
- [25] Hagelaar G J M and Pitchford L C 2005 *Plasma Sources Sci. Technol.* **14** 722–733
- [26] Tritton D J 1988 *Physical Fluid Dynamics* (Oxford University Press)
- [27] McDaniel E W and Mason E A 1973 *The mobility and diffusion of ions in gases* (Wiley)

- [28] Ferreira C M, Loureiro J and Ricard A 1985 *J. Appl. Phys.* **57** 82–90
- [29] Biagi database www.lxcat.net version 7.1, 2004, retrieved in February, 2020
- [30] Hyman H 1979 *Phys. Rev. A* **20** 855–859
- [31] Raizer Y P 1991 *Gas Discharge Physics* (Springer-Verlag)
- [32] Dyatko N A, Ionikh Y Z, Kochetov I V, Marinov D L, Meshchanov A V, Napartovich A P, Petrov F B and Starostin S A 2008 *J. Phys. D: Appl. Phys.* **41** 055204
- [33] Jonkers J, Van de Sande M, Sola A, Gamero A, Rodero A and van der Mullen J 2003 *Plasma Sources Sci. Technol.* **12** 464–474
- [34] Cunningham A J, O'Malley T F and Hobson R M 1981 *J. Phys. B: At. Mol. Phys.* **14** 773–782
- [35] Castaños-Martinez E, Kabouzi Y, Makasheva K and Moisan M 2004 *Phys. Rev. E: Stat. Nonlinear Soft Matter Phys.* **70** 066405
- [36] Gregório J, Leprince P, Boisse-Laporte C and Alves L L 2012 *Plasma Sources Sci. Technol.* **21** 015013
- [37] Bultel A, van Ootegem B, Bourdon A and Vervisch P 2002 *Phys. Rev. E: Stat. Nonlinear Soft Matter Phys.* **65** 046406
- [38] Lam S K, Zheng D, Lo A, Dem'yanov A and Napartovich A P 2000 *J. Phys. D: Appl. Phys.* **33** 242–251
- [39] Hagelaar G J M 2008 Modelling methods for low-temperature plasmas Tech. rep. Plasmas. Université Toulouse III Paul Sabatier (UT3 Paul Sabatier)